Maximizing Output Power of Inductive Power Transfer Systems Under Rebar Array Shielding

Yuner Peng, *Graduate Student Member, IEEE*, Endian Ma, Qi Wang, Yang Chen, *Senior Member, IEEE*, Ruikun Mai, *Senior Member, IEEE*, and Udaya K. Madawala, *Fellow, IEEE*

***Abstract*—Sensors in structural health monitoring systems can be wirelessly powered by Inductive power transfer (IPT) technology. However, wireless power transfer to sensors is significantly affected by the shielding effect of magnetic fields due to induced eddy currents in rebar arrays. This article presents a method to lower the equivalent impedance of rebar loops, which thereby transforms the rebar array from a shield to an intermediate relay coil to improve power transmission. The proposed method uses an additional coil mounted on the rebar, which is coupled with two adjacent rebar loops and connected in series with a capacitor. By modifying the capacitance value, the magnitude and phase of the induced current in the rebar array can be modified to increase the induced voltage in the receiver (RX) coil. The equivalent circuit model of the system is analyzed based on the dipole coil as the transmitter and RX coil. Furthermore, a parameter design method for capacitance in series with the additional coil is presented to enable the system to achieve maximum output power capacity. Experimental results showed that the proposed method elevates the output power from 0.15 to 2.67 W.**

***Index Terms*—Inductive power transfer, maximum output power improvement, rebar array.**

I. Introduction

RECENTLY, inductive power transfer (IPT) technology has gained significant attention and has been widely adopted in various commercial applications, including automated guided vehicles, electric vehicles, and consumer electronics [1], [2], [3], [4], [5], [6]. The convenience and flexibility of IPT technology have made it a popular choice for powering wireless sensor networks [7], [8], [9], particularly in combination with unmanned aerial vehicles or robots [10], [11], [12]. IPT technology has been especially beneficial in extending the lifespan of wireless sensors used in structural health monitoring (SHM) systems as they are embedded in concrete, and their batteries cannot be easily replaced [13], [14]. By utilizing IPT technology, these SHM systems, used in large structures such as bridges, tunnels, and dams, can be powered for a long time, thus making them more practical and commercially viable. As the demand for safer and more efficient infrastructure continues to grow, the use of IPT technology is expected to become increasingly important in ensuring the longevity and safety of these critical structures.

In contrast to most IPT systems that have air as the medium across which the power transfer takes place, the transmission medium of IPT systems used in SHM systems is concrete, containing rebar arrays, and has different degrees of attenuation and absorption of the transmitted power.

Concrete comprises cement, sand, aggregate, and water, which can cause dielectric loss and resonant frequency variation. The extent of these effects depends on the concrete mix proportion, the degree of moisture, the type of aggregate used, and the system frequency [15]. Currently, some studies have established loss models for concrete, which indicate no significant impact on the system when operating in the hundreds of kilohertz range [16], but significant power attenuation occurs when the frequency rises to tens of megahertz [17].

The rebar array used to increase the strength of concrete is made of metal bars that are welded together but it is well-known that these metals significantly impact the performance of IPT systems [18], [19], [20]. The conductive loop within the rebar array will exhibit eddy currents when subjected to an alternating magnetic field excitation, and these eddy currents will generate a magnetic field that cancels out the magnetic field produced by the transmitter (TX) coil current. This phenomenon is known as Faraday cage shielding [21]. As shown in Fig. 1, the magnetic field near the receiver (RX) coil underneath the rebar faces a sharp reduction in the magnetic field after shielding. The decrease in magnetic strength means a decrease in the equivalent mutual coupling, which results in a decrease in the maximum power output of the system. In [22], it is observed that placing the RX coil on the surface of the rebar resulted in a decrease in output power from 12 dBm (without rebar) to 1 dBm. Furthermore, an investigation focused on eddy current distribution within a double-layer rebar array through simulation was developed in [23]. The results demonstrate that the magnetic field near the

Manuscript received 3 November 2023; revised 19 February 2024 and 2 May 2024; accepted 14 June 2024. Date of publication 19 June 2024; date of current version 4 September 2024. This work was supported in part by the National Natural Science Foundation of China Joint Fund for Regional Innovation and Development under Grant U22A20222, in part by the Sichuan Nature and Science Foundation Innovation Research Group Project under Grant 2023NSFSC1975, and in part by the National Key Research and Development Program of China under Grant 2023YFB4302002. Recommended for publication by Associate Editor C. Lee. *(Corresponding author: Ruikun Mai.)*

Yuner Peng, Endian Ma, Qi Wang, Yang Chen, and Ruikun Mai are with the School of Electrical Engineering, Southwest Jiaotong University, Chengdu 611756, China (e-mail: pengyuner@my.swjtu.edu.cn; maendian2022212312@my.swjtu.edu.cn; wangqi2022@my.swjtu.edu.cn; yangchen@swjtu.edu.cn; mairk@swjtu.edu.cn).

Udaya K. Madawala is with the Department of Electrical and Computer Engineering, University of Auckland, Auckland 1010, New Zealand (e-mail: u.madawala@auckland.ac.nz).

Color versions of one or more figures in this article are available at https://doi.org/10.1109/TPEL.2024.3416546.

Digital Object Identifier 10.1109/TPEL.2024.3416546

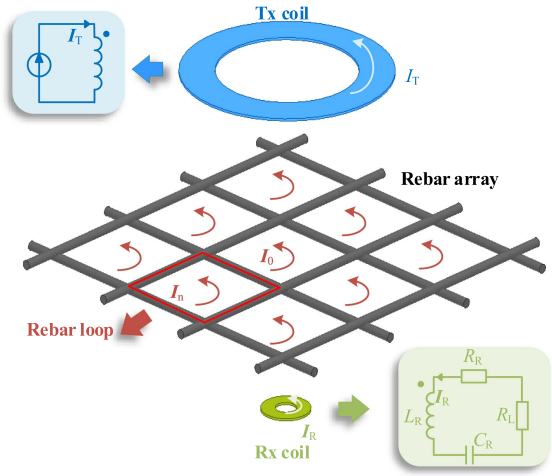

Fig. 1. Schematic of IPT system with rebar array shielding.

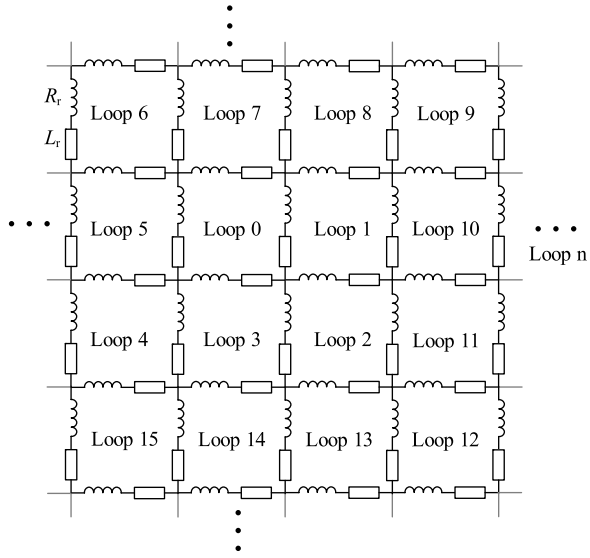

Fig. 2. Equivalent circuit of a rebar array.

bottom-layer rebar array decreases significantly to the extent that the generation of eddy currents becomes nearly absent following the shielding effect of the upper-layer rebar array.

Several attempts have also been made to mitigate the impact of the rebar array. In [24], a coil structure comprising a large and four small coils in series was proposed to increase mutual inductance. A multirelay IPT system installed on rebar columns was proposed in [25], which reduces eddy currents by installing coils inside rebar loops. These methods aim to minimize eddy current losses by designing the size and position of the coils with respect to the rebar array. In addition, Peng et al. [26] proposed a method utilizing eddy currents in the rebar array for wireless powering of sensors. However, this approach has limitations, as it can only supply power to the sensors located near the rebar array and is not applicable to sensors located beneath the rebar array.

In [27], the rebar array was modeled as multiple inductive coils to analyze its impact on the output voltage, indicating that the rebar loop impedance is a key factor limiting power transfer to the RX coil. This type of system can be effectively modeled by introducing unavoidable "coils" with shielding effects between the TX and RX coils. In some studies, passive shielding coils were introduced to reduce the electromagnetic field of IPT systems to the external environment [28], [29]. These shielding coils are typically configured to be inductive to optimize the shielding effectiveness by adjusting their impedance to manipulate the magnetic field distribution [30], [31]. The primary reason for shielding is that the phase of the induced eddy current in the inductive rebar loop opposes the TX coil current, resulting in a smaller magnetic field generated by the two currents compared to that generated by the original TX coil. Using this shielding concept, this article proposes a solution that uses additional auxiliary coils to modify the equivalent impedance of the rebar loops, with the aim of altering the phase of the induced eddy current. This adjustment enables the magnetic field due to the induced current to be effectively combined with the magnetic field generated by the TX coil, resulting in an increase in the maximum output power.

The rest of this article is organized as follows. Section II explains the equivalent circuits of the rebar array in detail. Then, the proposed system's structure and equivalent circuit are presented in Section III. In Section IV, the trend of the equivalent impedance of the rebar loop and the parameter design method for the maximum power output capability is derived. A prototype is constructed to verify the theoretical analysis in Section V. Finally, Section VI concludes this article.

II. Calculation of Rebar Current Distribution

The relative positions of the TX coil, RX coil, and rebar array of a wirelessly energized sensor embedded at a depth beyond the rebar array are shown in Fig. 1. The metallic rebar array is situated within the magnetic field region between the TX coil and the RX coil. Thus, eddy currents are generated in the rebar loops, shielding the magnetic field.

The rebar array is commonly constructed by welding multiple steel bars together. These bars possess conductive properties, allowing each rebar loop to act as a coil interconnected with others, and also to be magnetically coupled with the TX and RX coil. In [23], each rebar loop is represented as an inductor in series with parasitic resistance. However, a more realistic equivalent circuit model should consider the effect of the connections between the rebar on the distribution of rebar currents. Therefore, we established the equivalent circuit diagram of the rebar array, as shown in Fig. 2. Each short bar is represented as an inductor L_r in series with a parasitic resistance R_r. $\boldsymbol{I}_n$ represents the current of rebar loop "n," whose positive direction is defined in the same way as that of the TX and RX coils, as shown in Fig. 1.

In addition to being magnetically coupled with the TX and RX coils, the rebar loop is also magnetically coupled with the surrounding loop. We only consider the cross-coupling between

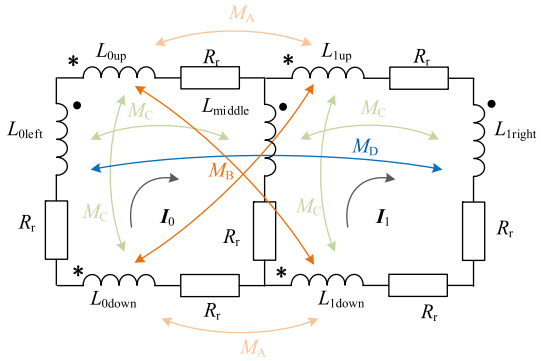

Fig. 3. Definition of mutual inductance between short bars.

adjacent coils, such as loop 0 and loop 1. The coupling between diagonal loops such as loop 0 and loop 2 is negligibly small. When considering the connection of rebars, the equivalent cross-coupled mutual inductance can be calculated based on the coupling between these short bars. The coupling between short bars of two adjacent loops is shown in Fig. 3. These mutual inductances can be divided into four categories, M_{A}, M_{B}, M_{C}, and M_{D}, according to the position relationship between the short bars. M_{A} is the mutual inductance between two connected bars, such as $L_{0\mathrm{up}}$ and $L_{1\mathrm{up}}$ that are in the same direction. M_{B} is the mutual inductance between two short bars that are parallel but located in different loops, such as $L_{0\mathrm{up}}$ and $L_{1\mathrm{down}}$. M_{C} is the mutual inductance between two parallel and adjacent bars, such as $L_{0\mathrm{up}}$ and $L_{0\mathrm{down}}$. M_{D} is the mutual inductance between two bars, such as $L_{0\mathrm{left}}$ and $L_{1\mathrm{right}}$, which are parallel and apart by one bar.

The induced voltage by $\boldsymbol{I}_1$ in loop 0 can be expressed as

$$V_{1\_to\_0} = j\omega \boldsymbol{I}_1 \left(2M_{\mathrm{A}} - 2M_{\mathrm{B}} + 2M_{\mathrm{C}} - M_D\right) - \left(j\omega L_{\mathrm{middle}} + R_{\mathrm{r}}\right) \boldsymbol{I}_1. \tag{1}$$

Since $L_{\mathrm{middle}} = L_{\mathrm{r}}$ and $\omega L_{\mathrm{middle}} >> R_{\mathrm{r}}$, (1) can be rewritten as

$$V_{1\_to\_0} \approx j\omega M_{\mathrm{EQ}} \boldsymbol{I}_1, \quad M_{\mathrm{EQ}} = 2M_{\mathrm{A}} - 2M_{\mathrm{B}} + 2M_{\mathrm{C}} - M_D - L_{\mathrm{middle}}. \tag{2}$$

According to Kirchhoff's voltage law, the relationship between currents of the TX, RX, and rebar loops can be obtained. M_{Tn} represents the mutual inductance between the TX coil and the nth rebar loop, while M_{Rn} denotes the mutual inductance between the RX coil and the $\mathrm{n_{th}}$ rebar loop. L_{R} represents the inductance of the RX, C_{R} represents the series compensation capacitor of the RX, and R_{R} represents the parasitic resistance of the RX

$$\boldsymbol{Z} \cdot \boldsymbol{I} = -j\omega \boldsymbol{I}_T \cdot \boldsymbol{M} \tag{3}$$

where

$$\boldsymbol{I} = \begin{bmatrix} \boldsymbol{I}_0 \\ \boldsymbol{I}_1 \\ \boldsymbol{I}_2 \\ \cdots \\ \boldsymbol{I}_{\mathrm{n}} \\ \boldsymbol{I}_{\mathrm{R}} \end{bmatrix}, \boldsymbol{M} = \begin{bmatrix} M_{\mathrm{T0}} \\ M_{\mathrm{T1}} \\ M_{\mathrm{T2}} \\ \cdots \\ M_{\mathrm{Tn}} \\ M_{\mathrm{TR}} \end{bmatrix}$$

$$\boldsymbol{Z} = \begin{bmatrix} Z_0 & Z_{01} & Z_{02} & & Z_{0\mathrm{n}} & j\omega M_{\mathrm{R0}} \\ Z_{01} & Z_1 & Z_{12} & \cdots & Z_{1\mathrm{n}} & j\omega M_{\mathrm{R1}} \\ Z_{02} & Z_{12} & Z_2 & & Z_{2\mathrm{n}} & j\omega M_{\mathrm{R2}} \\ & \cdots & & & \cdots & \cdots \\ Z_{0\mathrm{n}} & Z_{1\mathrm{n}} & Z_{2\mathrm{n}} & & Z_{\mathrm{n}} & j\omega M_{\mathrm{Rn}} \\ j\omega M_{\mathrm{R0}} & j\omega M_{\mathrm{R1}} & j\omega M_{\mathrm{R2}} & \cdots & j\omega M_{\mathrm{Rn}} & Z_{\mathrm{R}} \end{bmatrix}$$

$$Z_0 = Z_1 = \cdots = Z_n = j\omega L_{\mathrm{EQ}} + R_{\mathrm{EQ}}, L_{EQ} = 4L_r - 2M_C, R_{\mathrm{EQ}} = 4R_r$$

$$Z_{\mathrm{R}} = j\omega L_{\mathrm{R}} + 1/j\omega C_{\mathrm{R}} + R_{\mathrm{R}} + R_{\mathrm{L}}, \text{and} \omega = 2\pi f.$$

According to (2), the mutual impedance of adjacent rebar loops such as Z_{01} and Z_{03} can be expressed as

$$Z_{01} = Z_{03} = \ldots = j\omega M_{\mathrm{EQ}}. \tag{4}$$

The mutual impedance between other nonadjacent rebar loops, such as Z_{02} and Z_{04} can be considered 0

$$Z_{02} = Z_{04} = \ldots = 0. \tag{5}$$

By solving (6), $\boldsymbol{I}_{\mathrm{R}}$ and the currents of rebar loops can be obtained

$$\boldsymbol{I} = \boldsymbol{Z}^{-1} \cdot \left(-j\omega \boldsymbol{I}_T \cdot \boldsymbol{M}\right). \tag{6}$$

Moreover, the current in each bar can be obtained by subtracting the currents in two adjacent loops. Based on this, the impact of the rebar array on the IPT system can be investigated, as discussed in Section IV.

III. Proposed System

A. Structure

Fig. 4 shows the method proposed for changing the equivalent impedance of the rebar loops with an additional compact coil. As shown in Fig. 5, the dipole coil, which has been proven suitable for long-range sensor applications [32], [33], [34], [35], has been chosen for both TX and RX coils. The TX coil is located above the rebar array, while the RX coil is located below the rebar array. The TX and RX coils are aligned to achieve stronger magnetic coupling.

Rebar loop 0 and rebar loop 1 are opposite to the TX and RX coils, making them the most influential loops in the system. An additional coil in series with a compensation capacitor is placed between the rebar loop 0 and loop 1 and coupled with the two rebar loops. Thus, the equivalent impedance and current of the two coupled rebar loops ($\boldsymbol{I}_0$ and $\boldsymbol{I}_1$) can be changed by changing the capacitance value.

The winding of the additional coil, illustrated in Fig. 6, comprises two semitoroidal ferrite cores and a Litz wire. Ferrite

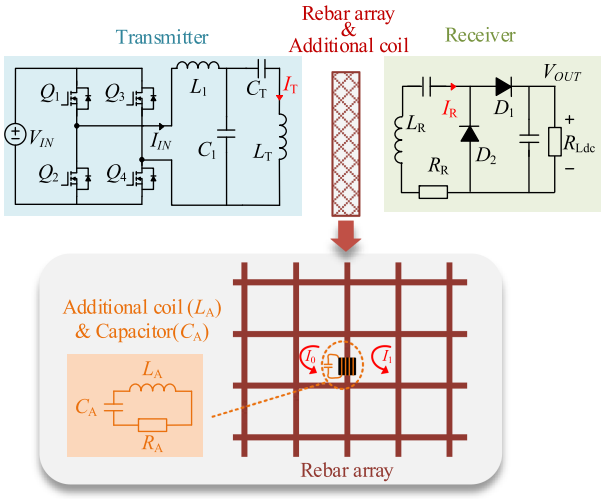

Fig. 4. Proposed system.

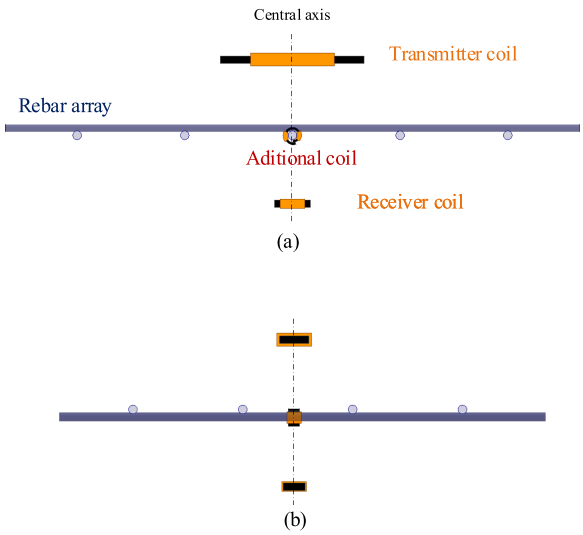

Fig. 5. TX coil, RX coil, and the additional coil. (a) Front view. (b) Right view.

cores are wrapped around the rebar, and the Litz wire is tightly wound around the magnetic core in the same direction.

B. Equivalent Circuit Analysis

As shown in Fig. 4, TX utilizes an *LCC* compensation topology consisting of L_1, C_1, and C_T. When $\omega L_1 = 1/\omega C_1 = \omega L_T\text{-}1/\omega C_T$, the current of the TX coil ($\boldsymbol{I}_T$) is maintained constant. Four MOSFET (Q_1–Q_4) and dc voltage sources constitute a high-frequency ac power supply. The RX coil is connected in series with a compensation capacitor C_R and connected to the load resistance R_{Ldc} through a half-bridge rectifier consisting of two diodes (D_1 and D_2).

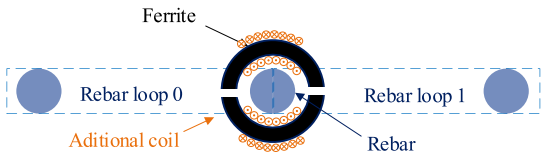

Fig. 6. Cross section of the additional coil.

The elements of each matrix in (3) need to be adjusted as additional coils are added. Regarding the small additional coil, its mutual inductance with the TX/RX coil is considerably smaller compared to the coupling with the rebar loop, and can be neglected. $\boldsymbol{I}$ and $\boldsymbol{M}$ can be rewritten as

$$\boldsymbol{I} = \begin{bmatrix} \boldsymbol{I}_0 \\ \boldsymbol{I}_1 \\ \boldsymbol{I}_2 \\ \cdots \\ \boldsymbol{I}_n \\ \boldsymbol{I}_A \\ \boldsymbol{I}_R \end{bmatrix}, \boldsymbol{M} = \begin{bmatrix} M_{T0} \\ M_{T1} \\ M_{T2} \\ \cdots \\ M_{Tn} \\ 0 \\ M_{TR} \end{bmatrix} \tag{7}$$

where $\boldsymbol{I}_A$ represents the current of the additional coil.

Since the ferrite is wrapped around the short bar between loop 0 and loop 1, the self-inductance of the bar will increase so that Z_0, Z_1, and Z_{01} change into Z_0', Z_1', and Z_{01}'. $\boldsymbol{Z}$ can be rewritten as (8) shown at the bottom of this page.

Due to the opposing flux flow generated by the additional coil through loop 0 and loop 1, both loop 0 and loop 1 own the same mutual inductances with the additional coil (M_A) but with different connection polarities. The equivalent reactance X_A of the additional coil L_A and the capacitor C_A is defined as $X_A = \omega L_A\text{-}1/\omega C_A$ while R_A represents the parasitic resistance of the additional coil.

$$\boldsymbol{Z} = \begin{bmatrix} Z_0' & Z_{01}' & Z_{02} & & Z_{0n} & j\omega M_A & j\omega M_{R0} \\ Z_{01}' & Z_1' & Z_{12} & \cdots & Z_{1n} & -j\omega M_A & j\omega M_{R1} \\ Z_{02} & Z_{12} & Z_2 & & Z_{2n} & 0 & j\omega M_{R2} \\ & \cdots & & & & \cdots & \cdots \\ Z_{0n} & Z_{1n} & Z_{2n} & \cdots & Z_n & 0 & j\omega M_{Rn} \\ j\omega M_A & -j\omega M_A & 0 & & 0 & jX_A + R_A & 0 \\ j\omega M_{R0} & j\omega M_{R1} & j\omega M_{R2} & & j\omega M_{Rn} & 0 & Z_R \end{bmatrix}$$

$$Z_0' = Z_1' = j\omega L_{EQ}' + R_{EQ}', Z_{01}' = j\omega M_{EQ}'. \tag{8}$$

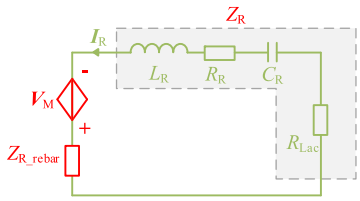

Fig. 7. Thevenin equivalent circuit on the RX side.

C. Thevenin Equivalent Circuit

For the system as proposed, there are too many loops to include in the calculations, and it is difficult to derive the analytic expression. Therefore, the Thevenin equivalent circuit is utilized to analyze the circuit characteristics. Applying Thevenin's theorem, the proposed system can be converted into its equivalent circuit on the RX side, as shown in Fig. 7. In this way, the impact of the TX coil, additional coil, and rebar array on the RX side is modeled as a voltage source $\boldsymbol{V}_{\mathrm{M}}$ in series with the impedance $Z_{\mathrm{R\_rebar}}$.

The $\boldsymbol{V}_{\mathrm{M}}$ can be obtained by treating the RX side as an open circuit. Substituting $Z_{\mathrm{R}} = \infty$ to (7), and (8) shown at the bottom of the next page into (6), the current in each loop can be given when the RX is open ($\boldsymbol{I}_{\mathrm{OPEN}}$)

$$\boldsymbol{I}_{\mathrm{OPEN}}|_{Z_{\mathrm{R}}=\infty} = \boldsymbol{Z}^{-1} \cdot (-j\omega \boldsymbol{I}_T \cdot \boldsymbol{M}). \tag{9}$$

Then, $\boldsymbol{V}_{\mathrm{M}}$ can be represented as a function of variable X_{A}

$$\boldsymbol{V}_{\mathrm{M}}(X_{\mathrm{A}}) = \begin{bmatrix} M_{\mathrm{R0}} & \cdots & M_{\mathrm{Rn}} & 0 & 0 \end{bmatrix} \cdot \boldsymbol{I}_{\mathrm{OPEN}}. \tag{10}$$

By setting the $\boldsymbol{I}_{\mathrm{T}}$ to zero and applying a voltage source ($\boldsymbol{V}_{\mathrm{ZERO}}$) to the RX, $Z_{\mathrm{R\_rebar}}$ can be calculated. In this case, the current of each loop ($\boldsymbol{I}_{\mathrm{ZERO}}$) can be obtained from

$$\boldsymbol{I}_{\mathrm{ZERO}}|_{\boldsymbol{I}_{\mathrm{T}}=0} = \boldsymbol{Z}^{-1} \cdot \begin{bmatrix} 0 & \cdots & \boldsymbol{V}_{\mathrm{ZERO}} \end{bmatrix}^T. \tag{11}$$

Based on the RX coil current ($\boldsymbol{I}_{\mathrm{R\_ZERO}}$) obtained in (11), $Z_{\mathrm{R\_rebar}}$ can be derived through

$$Z_{\mathrm{R\_rebar}}(X_{\mathrm{A}}) = \frac{\boldsymbol{V}_{\mathrm{ZERO}}}{\boldsymbol{I}_{\mathrm{R\_ZERO}}} - (j\omega L_{\mathrm{R}} + 1/j\omega C_{\mathrm{R}} + R_{\mathrm{R}}). \tag{12}$$

To achieve maximum output power, the value of C_{R} should be configured to cancel out the imaginary part of the impedance of $Z_{\mathrm{R\_rebar}}$ and $j\omega L_{\mathrm{R}}$

$$\mathrm{Im}\left(Z_{\mathrm{R\_rebar}}(X_{\mathrm{A}}) + j\omega L_R + 1/j\omega C_R\right) = 0. \tag{13}$$

IV. Equivalent Impedance Change Method

A. Analysis of Equivalent Impedance Change

The impedance of rebar loop 0 (Z_{EQ0}) is the ratio of the induced voltage of the rebar circuit to the rebar current $\boldsymbol{I}_0$

$$Z_{EQ0} = \frac{-j\omega M_{T0} \boldsymbol{I}_T}{\boldsymbol{I}_0}. \tag{14}$$

By utilizing the mutual inductance and rebar array parameters in Table I, the trajectory of Z_{EQ0}, and $\boldsymbol{V}_{\mathrm{M}}$ with X_{A} in the complex plane can be shown in Figs. 8 and 9. As X_{A} approaches $-\infty$ and $+\infty$, the additional coil is in an open circuit situation, and the

TABLE I
Values of System and Component Parameters

Parameter	Value	Parameter	Value
L_1	4.1 μH	C_1	97.3 nF
C_T	2.3 nF	L_T	178.2 μH
L_{EQ}	360 nH	L_{EQ}'	506 nH
M_{TR}	1.18 μH	M_A	2.62 μH
M_{EQ}	-64 nH	M_{EQ}'	-210 nH
R_{EQ}	0.12 Ω	R_{EQ}'	0.12 Ω
M_{T0}	417 nH	M_{T1}	-417 nH
M_{T2}	-87 nH	M_{T3}	87 nH
M_{T4}	54 nH	M_{T5}	151 nH
M_{T6}	54 nH	M_{T7}	87 nH
M_{T8}	-87 nH	M_{T9}	-54 nH
M_{T10}	-151 nH	M_{T11}	-54 nH
M_{T12}	-9 nH	M_{T13}	-6 nH
M_{T14}	6 nH	M_{T15}	9 nH
M_{R0}	224 nH	M_{R1}	-224 nH
M_{R2}	-28 nH	M_{R3}	28 nH
M_{R4}	11 nH	M_{R5}	23 nH
M_{R6}	11 nH	M_{R7}	28 nH
M_{R8}	-28 nH	M_{R9}	-11 nH
M_{R10}	-23 nH	M_{R11}	-11 nH
M_{R12}	-2 nH	M_{R13}	-2 nH
M_{R14}	2 nH	M_{R15}	2 nH
L_A	53.7 μH	R_A	0.42 Ω
L_R	171.4 μH	R_R	0.96 Ω
C_A	10.76 nF	C_R	2.358 nF
C_R'	2.349 nF	f	250 kHz

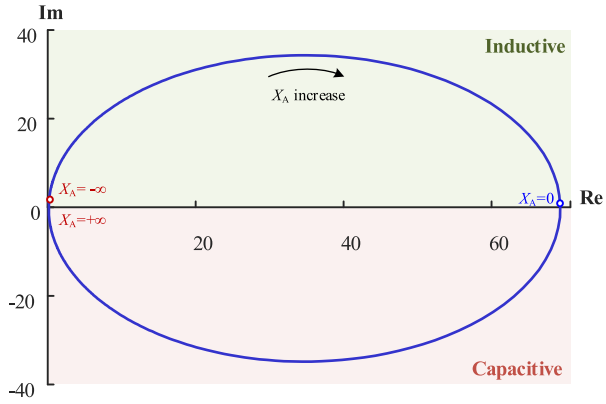

Fig. 8. Distribution of Z_{EQ0} in the complex plane with X_{A}.

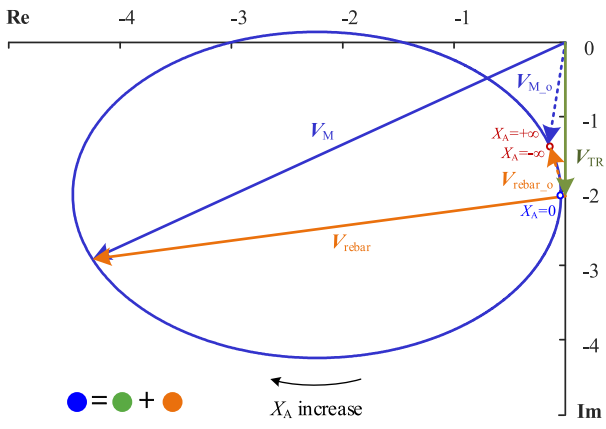

Fig. 9. Distribution of $\boldsymbol{V}_{\mathrm{M}}$ in the complex plane with X_{A}.

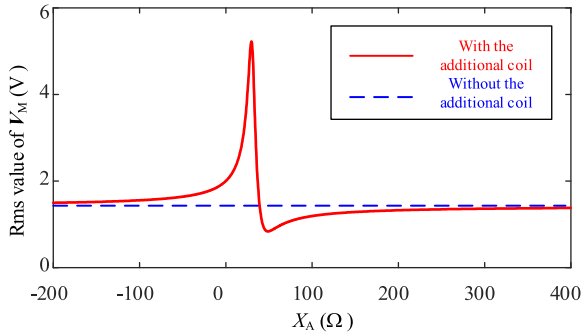

Fig. 10. Rms value of $\boldsymbol{V}_{\mathrm{M}}$ with X_{A}.

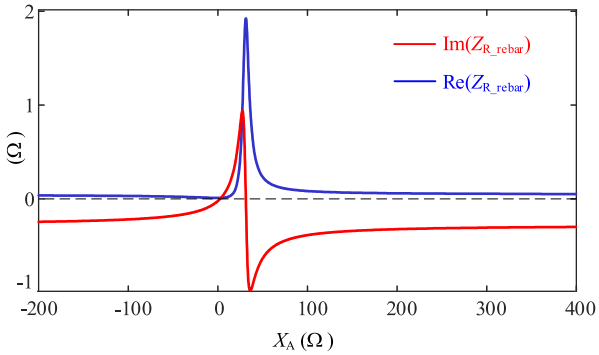

Fig. 11. Real and imaginary parts of $Z_{\mathrm{R\_rebar}}$ with X_{A}.

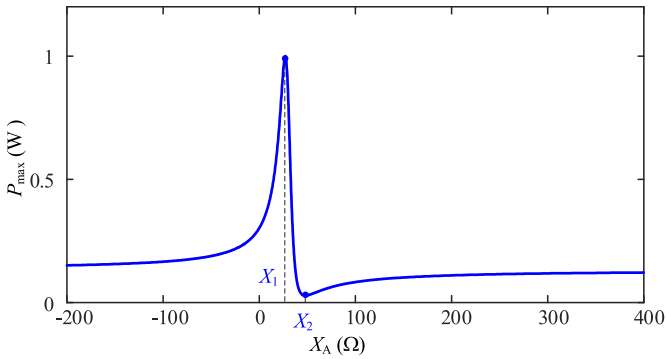

Fig. 12. Calculated $P_{\max}$ with X_{A}.

system is almost equivalent to without the additional coil, as shown by red points in Figs. 8 and 9. In this case without the additional coil, Z_{EQ0} approximates to a pure inductance. As X_{A} increases, Z_{EQ0} moves from the first quadrant to the fourth and back again. In other words, Z_{EQ0} changes from inductive to capacitive and finally to inductive again.

$\boldsymbol{V}_{\mathrm{M}}$ is the vector sum of the induced voltage generated by the TX coil current ($\boldsymbol{V}_{\mathrm{TR}}$)and the induced voltage generated by the rebar loop currents ($\boldsymbol{V}_{\mathrm{rebar}}$), as shown in Fig. 9

$$\boldsymbol{V}_{\mathrm{M}} = \boldsymbol{V}_{\mathrm{TR}} + \boldsymbol{V}_{\mathrm{rebar}} \tag{15}$$

$$\boldsymbol{V}_{\mathrm{TR}} = -j\omega M_{\mathrm{TR}} \boldsymbol{I}_T, \boldsymbol{V}_{\mathrm{rebar}} = -j\omega \sum_{n=0}^{n} M_{\mathrm{Rn}} \boldsymbol{I}_n. \tag{16}$$

Since the $\boldsymbol{I}_{\mathrm{T}}$ is constant, the $\boldsymbol{V}_{\mathrm{TR}}$ is constant, as the green vector shown in Fig. 9. $\boldsymbol{V}_{\mathrm{rebar}}$ is represented by the orange vector and $\boldsymbol{V}_{\mathrm{M}}$ is represented by the blue vector. When X_{A} approaches $-\infty$ and $+\infty$, the vector of dashed lines ($\boldsymbol{V}_{\mathrm{M\_o}}$ and $\boldsymbol{V}_{\mathrm{rebar\_o}}$) is used to distinguish between different cases.

The magnitude and phase difference between $\boldsymbol{V}_{\mathrm{rebar}}$ and $\boldsymbol{V}_{\mathrm{TR}}$ changes with Z_{EQ0}. When Z_{EQ0} is inductive, $\boldsymbol{V}_{\mathrm{rebar}}$ is in the opposite direction of $\boldsymbol{V}_{\mathrm{TR}}$, resulting in the rms value of $\boldsymbol{V}_{\mathrm{M}}$ being smaller than $\boldsymbol{V}_{\mathrm{TR}}$ after vector sum, as a dashed blue vector in Fig. 9. However, when Z_{EQ0} is capacitive, the component of $\boldsymbol{V}_{\mathrm{rebar}}$ in the direction of $\boldsymbol{V}_{\mathrm{TR}}$ is positive. Especially when Z_{EQ0} is minimal and approaches resistive characteristics, the induced current in rebar loop 0 becomes relatively large, resulting in a greater $\boldsymbol{V}_{\mathrm{rebar}}$. Simultaneously, the direction of $\boldsymbol{V}_{\mathrm{rebar}}$ no longer opposes $\boldsymbol{V}_{\mathrm{TR}}$. Consequently, the rms value of $\boldsymbol{V}_{\mathrm{M}}$ exceeds $\boldsymbol{V}_{\mathrm{TR}}$ after vector superposition, shown as a solid blue vector in Fig. 9.

Fig. 10 shows the trend of $\boldsymbol{V}_{\mathrm{M}}$ rms changing with X_{A}, and it can be seen that the appropriate value of X_{A} can significantly increase the equivalent voltage at the RX side.

B. Parameter Optimal Design

However, any variation in X_{A} results in a corresponding alteration in $Z_{\mathrm{R\_rebar}}$, as illustrated in Fig. 11, which, in turn, impacts the output power. To achieve the maximum output power, the impedance of the imaginary part of $Z_{\mathrm{R\_rebar}}$ should be canceled out entirely by C_{R} and L_{R}. Similarly, a large real part of $Z_{\mathrm{R\_rebar}}$ (Re($Z_{\mathrm{R\_rebar}}$)) will cause a small voltage drop across the load resistance, resulting in a small amount of power the system can output. Therefore, to maximize the system's output power capacity, X_{A} needs to be configured, carefully considering both $\boldsymbol{V}_{\mathrm{M}}$ and Re($Z_{\mathrm{R\_rebar}}$).

Based on the derivation in [26], output power, including the impact of diodes, can be expressed as

$$P_{\mathrm{R\_OUT}}(X_{\mathrm{A}}, R_{\mathrm{Ldc}}) = \frac{2R_{\mathrm{Ldc}}}{\pi^2} \frac{\left(|\boldsymbol{V}_{\mathrm{M}}(X_A)| - \frac{2\sqrt{2}}{\pi} V_{\mathrm{d}}\right)^2}{\left|\frac{2R_{\mathrm{Ldc}}}{\pi^2} + \mathrm{Re}\left(Z_{\mathrm{R\_rebar}}(X_A)\right) + R_{\mathrm{R}}\right|^2}. \tag{17}$$

When V_{d} is assumed to be a fixed value, the R_{Ldc} that maximizes the output power can be obtained by solving a zero-partial derivation of $P_{\mathrm{R\_OUT}}(X_{\mathrm{A}}, R_{\mathrm{Ldc}})$ with respect to R_{Ldc}

$$\frac{\partial P_{\mathrm{R\_OUT}}(X_{\mathrm{A}}, R_{\mathrm{Ldc}})}{\partial R_{\mathrm{Ldc}}} = 0. \tag{18}$$

By solving (18)

$$R_{\mathrm{Ldc\_op}} = \frac{\pi^2}{2}\left(\mathrm{Re}\left(Z_{\mathrm{R\_rebar}}(X_A)\right) + R_{\mathrm{R}}\right). \tag{19}$$

Substituting (19) into (17), the maximum output power can be written as a function of X_{A} ($P_{\max}$ (X_{A})). The relationship between X_{A} and the maximum power $P_{\max}$ is shown in Fig. 12. As X_{A} approaches $-\infty$ and $+\infty$, $P_{\max}$ is close to the original value (without the additional coil). Moreover, there are two peaks X_1 and X_2, one corresponding to the maximum point and the other to the minimum point. By solving (20), two peaks can

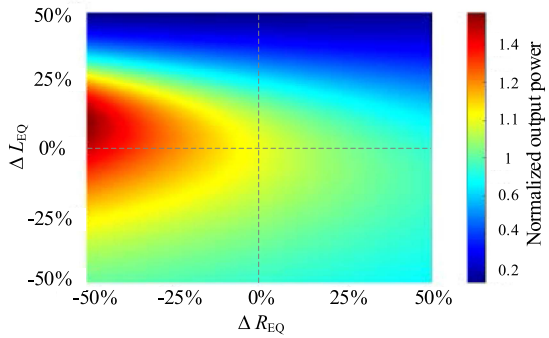

Fig. 13. Normalized calculated output power with variation of L_{EQ} and R_{EQ}.

be obtained

$$\frac{dP_{\max}(X_A)}{dX_A} = 0 \Rightarrow X_1, X_2. \tag{20}$$

To identify the maximum point, we can take the second derivative of $P_{\max}$ with respect to X_A. After substituting the given parameters into the equation, we can determine, which of X_1 and X_2 satisfies the condition in (21) and, thus, corresponds to the optimal value (X_{A_OP})

$$\frac{d^2P_{\max}(X_A)}{dX_A{}^2} < 0. \tag{21}$$

C. Aging Consideration

When the rebar array is embedded within concrete, aging can occur, causing changes in the self-inductance and internal resistance of the rebar loop, thereby affecting the output power. Fig. 13 simulates the normalized variations in calculated output power under ±50% changes in only L_{EQ} and R_{EQ}, while keeping other parameters constant. The power under unchanged parameters is used as the reference, denoted as 1. It is important to note that when considering parameter variations in the rebar array, all loops should be taken into account, not just loop0 and loop1. Therefore, the inductance L_{EQ} of the rebar loop without the additional coil is more representative and used for plotting and analysis. Since the presence of a magnetic core results in L_{EQ}' of the rebar loop with additional coils slightly larger than L_{EQ}, when L_{EQ} changes, L_{EQ}' used for calculation also changes accordingly. The difference between L_{EQ}' and L_{EQ} originates from the self-coupling magnetic field enhancement caused by the magnetic material of the additional coil, rather than aging. Hence, it is considered to keep the difference between the two unchanged during calculation.

It can be observed that as R_{EQ} decreases, the output power increases. This is because a smaller R_{EQ} allows for a larger current to flow in the rebar loop. When the change rate of R_{EQ} is 0%, both increasing and decreasing L_{EQ} will result in a decrease in output power. However, an increase in L_{EQ} leads to a significant decrease in output power, whereas a decrease in L_{EQ} results in a relatively slower decrease in output power. This is because an increase in L_{EQ} causes the rebar loop to approach more towards inductive with the shielding effect.

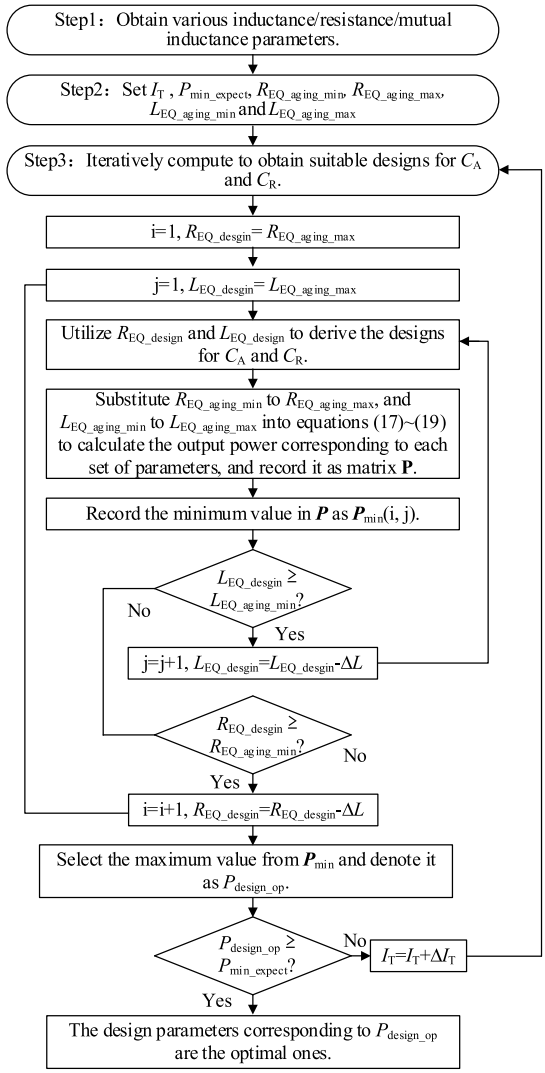

Fig. 14. Design flow with concerning rebar aging.

It should be noted that each set of R_{EQ} and L_{EQ} corresponds to its X_A to achieve maximum output power. Therefore, it is not feasible to achieve the theoretical maximum power under all variations of R_{EQ} and L_{EQ} with a fixed X_A. However, through appropriate design, the output power can be relatively high and acceptable under varying parameter conditions. If we consider a narrower range of ±20% for L_{EQ} and R_{EQ} variations, the lowest output power is 0.65 times the power when L_{EQ} and R_{EQ} remain unchanged. Although this represents a significant decrease, it still exceeds the power achieved without employing this method under shielding conditions.

Fig. 14 provided a design flow considering parameter variations. Through an iterative method, we obtain a design where the lowest output power during aging remains higher than the set boundary value P_{min_expect}. The first step involves obtaining the parameters of inductance, resistance, and mutual inductance in the system after determining the coupling mechanism design.

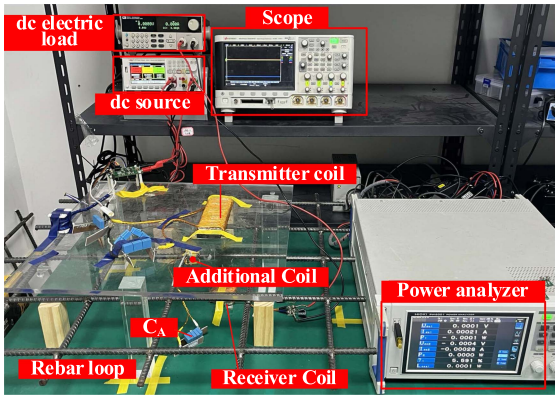

Fig. 15. Experimental setup.

The second step is to set the initial current value of the TX coil, the expected minimum power value P_{min_expect} during aging, and the expected boundaries of R_{EQ} and L_{EQ} ($R_{EQ\_aging\_min}$, $R_{EQ\_aging\_max}$, $L_{EQ\_aging\_min}$, and $L_{EQ\_aging\_max}$) during aging. The third step involves iterating through different R_{EQ} and L_{EQ} values as design references (R_{EQ_desgin}, L_{EQ_desgin}) to calculate the minimum output power during aging, and finding the maximum value (P_{design_op}) among all the minimum values ($\mathbf{P}_{min}$) corresponds to the optimal parameter design.

V. Experimental Validation

A. Experimental Prototype

To validate the proposed concept, a 250-kHz IPT system was built, as shown in Fig. 15. The MOSFETS Q_1-Q_2 were BSC146N10LS5, and the rectifier diodes D_1-D_2 were of PMEG3050EP type. The dc load resistance was emulated by an electronic load (IT8812C). The primary inverter of the system, fed by an 8-V source, was connected to an *LCC* compensation network to maintain a constant TX coil current of 1.1 A. The system frequency is set at 250 kHz. HIOKI (PW6001) power analyzer was utilized for power and efficiency measurements.

The rebar array was constructed with a kind of seismic rebar (HRB400) that meets Chinese national standards and is typically used in large structures. A total of ten 12 mm diameter HRB400 rebars were welded horizontally and vertically with a spacing of 15 cm to form a 4×4-grid rebar array. The distance between the rebar array and both the TX and RX coils is 10 cm, while the total transmission gap is 20 cm.

As depicted in Fig. 16, both the TX and RX coils are dipole coils consisting of Litz wire wrapped around ferrite. The size of TX ferrite is 20 cm×5 cm×1 cm. In order to fit the practical application for the SHM system, the size of the RX ferrite is smaller, only 5 cm×5 cm×1 cm. The number of turns of the TX coil is 30, and the number of turns of the RX coil is 40. The structure of the additional coil aligns with the description in Section III. The additional coil is wound by a 20-turn Litz wire around the ferrite core and then wrapped around the rebar. The ferrite core of the additional coil consists of two semitoroidal ferrites separated by two gaps of 1.5 mm, as illustrated in Fig. 14(c). The inner diameter of the ring core is 20 mm, with a

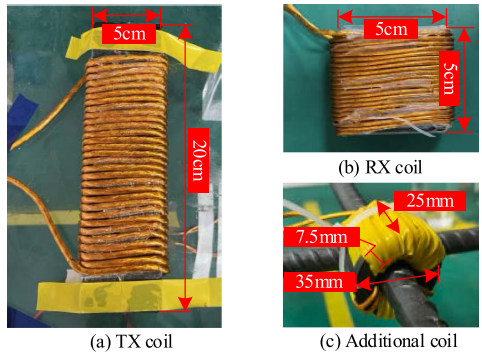

(a) TX coil (b) RX coil (c) Additional coil

Fig. 16. Photos of the TX, RX, and additional coil.

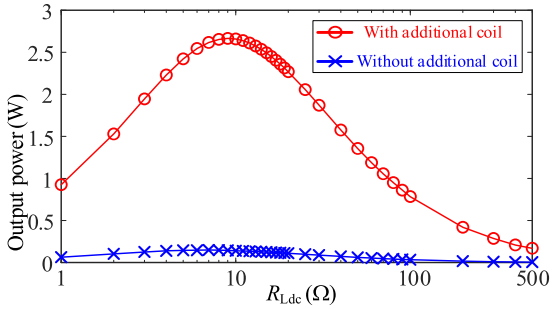

Fig. 17. Measured output power with R_{Ldc}.

TABLE II
Power Analyzer Test Result at Maximum Power

	Without additional coil	With additional coil
V_{IN}	8 V	8 V
V_{OUT}	1.04 V	4.92 V
$P_{R\ OUT}$	0.15 W	2.67 W
Efficiency	6.95%	34.79%

thickness of 7.5 mm, resulting in an outer diameter of 35 mm, and a width along the direction of the rebar of 25 mm. The TX coil Litz wire consists of 3000 strands of AWG24, while the RX and additional coil Litz wire comprises 300 strands of AWG24. The two semitoroidal ferrite cores are custom-made from PC95 material. Other system parameters are presented in Table I.

B. Experimental Result

In order to verify the effectiveness of the additional coil, experiments were performed with and without the additional coil. Fig. 17 depicts measured output power with R_{Ldc} in two states. Table II compares these two states at maximum output power. When there is no additional coil, the output power is relatively small, only 0.15 W (@7 Ω), as shown in the red line in Fig. 17. When with the additional coil, the output power is significantly increased to a maximum of 2.67 W (@9 Ω).

Fig. 18 shows both efficiency and output power with R_{Ldc}. The system efficiency and output voltage with the additional coil are higher than the state without the additional coil over the full range of R_{Ldc} from 1 to 500 Ω. The additional coil increases the maximum output dc voltage from 2.21 to 9.69 V (@500 Ω),

TABLE III
COMPARISON WITH OTHER METHODS

Proposed in	Ref. [26]	Ref. [22]	Ref. 24]	This work
Method description	Utilizing rebar eddy currents	Isolating with ferrite	Multi coil	Changing rebar loop equivalent impedance
Operating frequency	85 kHz	13.5 MHz	82.3 kHz	250 kHz
TX dimension	200 mm×200 mm	80 mm×80 mm	300 mm×300 mm	50 mm×200 mm
RX dimension	15 mm wide /5 mm high in cross-section	145.5 mm×45 mm	300 mm×300 mm	50 mm×50 mm
RX location	Fixed on rebar	Attaching to rebar	Under rebar array	Under rebar array
Gap	100 mm	20 mm	300 mm	200 mm
Initial power	0.84 W	-32 dBm	/	0.15 W
Maximum power (after improving)	1.957 W	1 dBm (1.256 mW)	10 W	2.67 W
Efficiency (@maximum power)	18.68%	0.1256%	39%	34.79%
Output voltage	5V	/	3.3 V	4.92 V

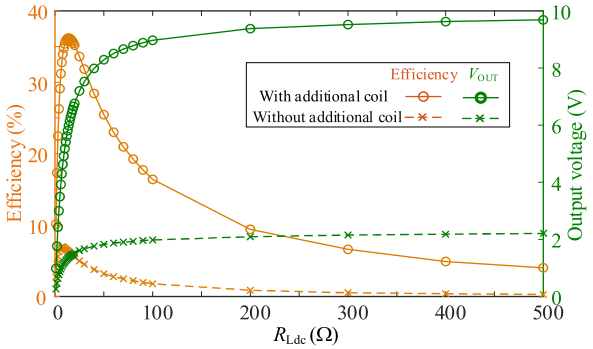

Fig. 18. Measured efficiency and V_{OUT} with R_{Ldc}.

a fourfold increase, indicating that the proposed method can significantly improve voltage gain and output power under the shielding of the rebar array. The peak efficiency during the entire load variation process occurs at a load of 14 Ω, with an efficiency of 36.18%. The efficiency at the point of maximum power corresponds to 34.79% (@9 Ω).

The waveforms of $\boldsymbol{I}_{\mathrm{T}}$, $\boldsymbol{I}_{\mathrm{R}}$, V_{out}, and the current ($\boldsymbol{I}_{\mathrm{REBAR}} = \boldsymbol{I}_0$-$\boldsymbol{I}_1$) of the rebar, where the additional coil was mounted, in Fig. 19 clearly show the variations in both the phase and magnitude of the current. Fig. 19(a) corresponds to the case of maximum output power without the additional coil, and Fig. 19(d) corresponds to the case of maximum output power with the additional coil. Theoretically, the induced voltage of the rebar loop lags behind $\boldsymbol{I}_{\mathrm{T}}$ by 90°. Experimental results reveal that in the absence of the additional coil, $\boldsymbol{I}_{\mathrm{Rebar}}$ exhibits a 180-degree phase lag with respect to $\boldsymbol{I}_{\mathrm{T}}$, indicating the inductive nature of the rebar loop's equivalent impedance. $\boldsymbol{I}_{\mathrm{Rebar}}$ and $\boldsymbol{I}_{\mathrm{T}}$ exhibit opposite phase angles, leading to the shielding effect, which manifests as low induced voltage. As a result, the induced voltage on the RX side decreases, giving rise to the phenomenon known as the shielding effect. When an additional coil is present, designed with parameters that maximize output power, $\boldsymbol{I}_{\mathrm{Rebar}}$ exhibits a lag of 71° with respect to $\boldsymbol{I}_{\mathrm{T}}$. In this case, the rebar loop manifests as a complex impedance with resistive and capacitive components. At the same time, due to partial compensation, the equivalent impedance of the rebar loop decreases, which also greatly increases the rebar current, as shown as the yellow wave in Fig. 19(d). The intervention of the additional coil alters the phase relationship between $\boldsymbol{I}_{\mathrm{rebar}}$ and $\boldsymbol{I}_{\mathrm{T}}$ from 180° to an acute angle, facilitating an effective superposition of their effects. As a result, they collectively contribute to strengthening the magnetic field on the RX side, enhancing the output power.

This study primarily focused on reducing the shielding effect of the rebar array. Concrete, as another transmission medium in SHM applications, has been found to have negligible effects on wireless power transfer within the range of tens to 250 kHz [16]. If the proposed method is applied in the MHz or higher frequency range, considerations for concrete attenuation and parasitic parameters may arise, necessitating further analysis.

C. Comparison

The proposed system was compared with other IPT systems that take rebar into consideration, as outlined in Table III. In [26], a method utilizing rebar eddy currents to deliver power to sensors near the rebar array was introduced. Appropriate compensation parameter design increased the output power from 0.84 W to 1.957 W. In [22], using a ferrite pad to separate the RX coil from direct contact with rebar increased the output power from −32 dBm to 1 dBm. While both methods effectively enhanced output power, they focused on transferring energy to the vicinity of the rebar array rather than improving the ability to transfer through it. Jang et al. [24] proposed a composite coil to enhance the coupling, reducing the shielding effect of the rebar and improving the energy penetration capabilities. However, to achieve the desired effect of the coil combination, the dimensions of the small coils within the composite coil need to match the rebar loop, resulting in an overall size of 300×300 mm. In contrast, this study aimed to reduce the shielding effect or even transform the rebar array into an energy relay by changing the equivalent impedance of the rebar array itself. Even with an RX coil size of only 50 mm×50 mm, significant power enhancement can be achieved. In practical applications, a smaller-sized RX is more suitable for installation, with a minimal impact on structural strength, making it a more viable solution.

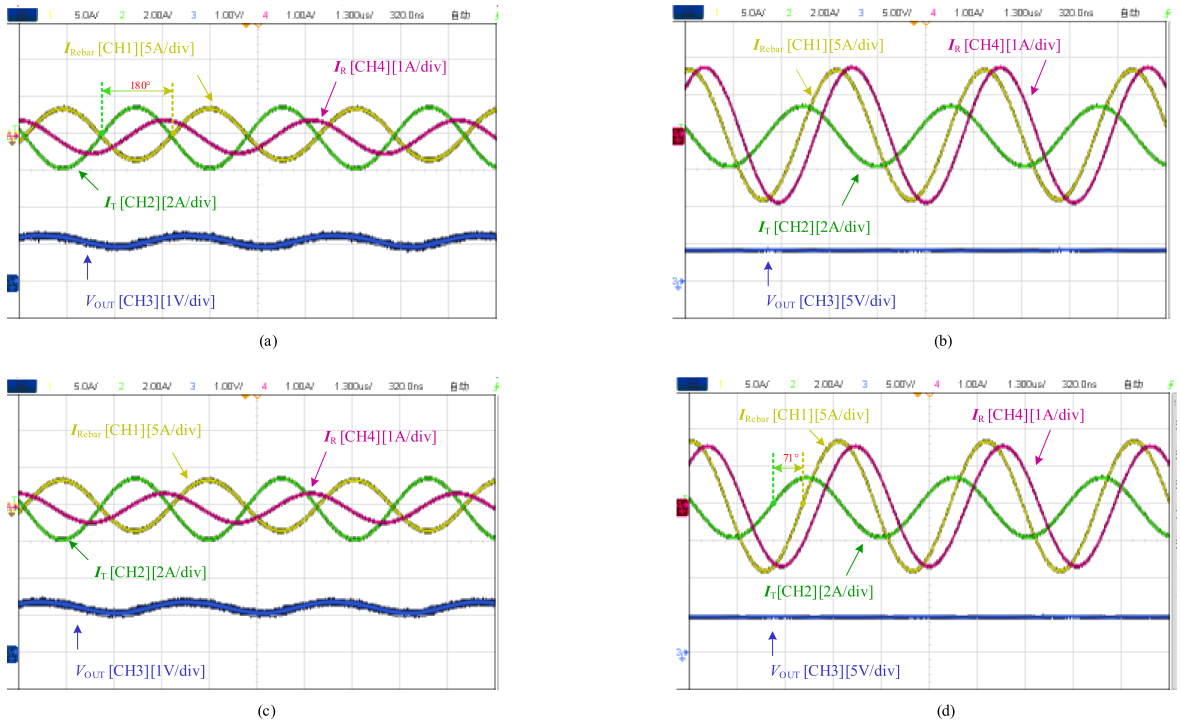

Fig. 19. Waveform of $\boldsymbol{I}_{\mathrm{T}}$, $\boldsymbol{I}_{\mathrm{R}}$, $\boldsymbol{I}_{\mathrm{Rebar}}$, and V_{OUT}. (a) Without additional coil (R_{Ldc}=7 Ω). (b) With additional coil. (c) Without additional coil (R_{Ldc}=9 Ω). (d) With additional coil (R_{Ldc}=9 Ω).

D. Discussion

When considering the practical issue of applying IPT for SHM systems, one must address the fact that the RX is hidden within the concrete. Aligning the TX and RX coils is necessary to achieve optimal output power. This consideration applies not only to the proposed methodology in this article but also to any IPT system implemented for SHM sensors. In this study, additional coils are installed on the rebar, while the RX coil remains fixed. Thus, the challenge becomes how to align the TX coil with the target rebar.

One viable approach involves determining the position of the target rebar through predesigned blueprints and key reference positions in the engineering project. Once the concrete has been set for 24 h, markings can be made on its surface. This is feasible due to the fixed positioning of the rebar as dictated by the initial design. The TX may be installed on automated devices such as robots or drones, or portable manual operation equipment. Using methods such as image recognition technology or visual observation, the TX can be aligned with the designated markings.

Furthermore, with emerging coil location identification techniques based on IPT system characteristics, more precise methods for coil positioning may be available in the future. These possibilities warrant further exploration.

VI. Conclusion

In this article, a method to enhance the maximum output power of IPT systems used in SHM applications was proposed. The method utilizes the rebar array as an intermediate relay coil by using a compact additional coil connected in series with a capacitor and enveloped around the rebar positioned between the TX and RX coils. An equivalent circuit of the system was presented, showing that the equivalent impedance of the rebar loops can be modified through the adjustment of the capacitance value to enhance power transfer to the RX. A design method for the selection of capacitance in series with the additional coil was also presented to achieve maximum output power. The analysis indicates that when the impedance of the rebar loops is adjusted to approach near-pure resistive with a capacitive component, there is a significant improvement in the induced voltage at the RX coil. Experimental results of a prototype system were presented to show that the output power can be effectively elevated from 0.15 to 2.67 W using the proposed method.

However, in actual structures, more complex rebar arrays may exist, which could involve multiple layers or even intricate multilayer cages. The magnetic field is further shielded by these additional layers of rebar, adding to the complexity of the problem. Consequently, questions arise: How should the number of additional coils be determined? How can the impedances of multiple additional coils be designed simultaneously? How will the equivalent impedance of the rebar loop be affected? Moreover, the interaction between different layers needs to be taken into account. The method proposed in this article cannot be directly applied to multilayer rebar arrays. Nevertheless, the concept of altering the equivalent impedance of the rebar array, as proposed in the article, provides valuable insights for multilayer configurations design where the lowest. In the future, research on the shielding effects of more complex rebar structures is imperative.

REFERENCES

[1] Y. Chen et al., "A clamp circuit-based inductive power transfer system with reconfigurable rectifier tolerating extensive coupling variations," *IEEE Trans. Power Electron.*, vol. 39, no. 2, pp. 1942–1946, Feb. 2024.

[2] C. Zhu et al., "A magnetic field concentration enhanced I-shaped transmitter for DWPT system to achieve low power fluctuation," *IEEE Trans. Power Electron.*, vol. 39, no. 1, pp. 1690–1700, Jan. 2024.

[3] H. Wang, Y. Wu, X. Li, X. Dai, Y. Sun, and J. Hu, "Advanced magnetic coupler design with multi-directional anti-misalignment capabilities for wireless charging unmanned aerial vehicles," *IEEE Trans. Circuits Syst. II, Exp. Briefs*, vol. 71, no. 6, pp. 3231–3235, Jun. 2024.

[4] C. Cai, J. Wang, M. Saeedifard, P. Zhang, R. Chen, and J. Zhang, "Gyrator-gain variable WPT topology for MC-unconstrained CC output customization using simplified capacitance tuning," *IEEE Trans. Ind. Electron.*, vol. 71, no. 4, pp. 3594–3605, Apr. 2024.

[5] U. K. Madawala and D. J. Thrimawithana, "A bidirectional inductive power interface for electric vehicles in V2G systems," *IEEE Trans. Ind. Electron.*, vol. 58, no. 10, pp. 4789–4796, Oct. 2011.

[6] Y. Zhang, S. Chen, X. Li, and Y. Tang, "Design methodology of free positioning nonoverlapping wireless charging for consumer electronics based on antiparallel windings," *IEEE Trans. Ind. Electron.*, vol. 69, no. 1, pp. 825–834, Jan. 2022.

[7] J. Chen, S. Li, S. Chen, S. He, and Z. Shi, "Q-charge: A quadcopter based wireless charging platform for large-scale sensing applications," *IEEE Netw.*, vol. 31, no. 6, pp. 56–61, Nov./Dec. 2017.

[8] B. H. Choi, E. S. Lee, Y. H. Sohn, G. C. Jang, and C. T. Rim, "Six degrees of freedom mobile inductive power transfer by crossed dipole Tx and rx coils," *IEEE Trans. Power Electron.*, vol. 31, no. 4, pp. 3252–3272, Apr. 2016.

[9] E. S. Lee, J. S. Choi, H. S. Son, S. H. Han, and C. T. Rim, "Six degrees of freedom wide-range ubiquitous IPT for IoT by DQ magnetic field," *IEEE Trans. Power Electron.*, vol. 32, no. 11, pp. 8258–8276, Nov. 2017.

[10] U. Baroudi, "Robot-assisted maintenance of wireless sensor networks using wireless energy transfer," *IEEE Sensors J.*, vol. 17, no. 14, pp. 4661–4671, Jul. 2017.

[11] S. Suman, S. Kumar, and S. De, "UAV-assisted RFET: A novel framework for sustainable WSN," *IEEE Trans. Green Commun. Netw.*, vol. 3, no. 4, pp. 1117–1131, Dec. 2019.

[12] J. M. Arteaga, P. D. Mitcheson, and E. M. Yeatman, "Development of a fast-charging platform for buried sensors using high frequency IPT for agricultural applications," in *Proc. IEEE Appl. Power Electron. Conf. Expo.*, 2022, pp. 1116–1121.

[13] C. A. Tokognon, B. Gao, G. Y. Tian, and Y. Yan, "Structural health monitoring framework based on Internet of Things: A survey," *IEEE Internet Things J.*, vol. 4, no. 3, pp. 619–635, Jun. 2017.

[14] G. Loubet, J.-P. Balayssac, A. Sidibe, D. Dragomirescu, and A. Takacs, "Battery-free, wirelessly powered and controlled concrete resistivity sensing node," in *Proc. Wireless Power Week*, 2022, pp. 547–552.

[15] F. Li, X. Sun, S. Zhou, Y. Chen, Z. Hao, and Z. Yang, "Infrastructure material magnetization impact assessment of wireless power transfer pavement based on resonant inductive coupling," *IEEE Trans. Intell. Transp. Syst.*, vol. 23, no. 11, pp. 22400–22408, Nov. 2022.

[16] F. Chen, N. Taylor, R. Balieu, and N. Kringos, "Dynamic application of the inductive power transfer (IPT) systems in an electrified road: Dielectric power loss due to pavement materials," *Construction Building Mater.*, vol. 147, pp. 9–16, Aug. 2017.

[17] S. Jiang and S. V. Georgakopoulos, "Optimum wireless powering of sensors embedded in concrete," *IEEE Trans. Antennas Propag.*, vol. 60, no. 2, pp. 1106–1113, Feb. 2012.

[18] C. Van Pham, A.-V. Pham, and C. S. Gardner, "Development of helical circular coils for wireless through-metal inductive power transfer," in *Proc. IEEE Wireless Power Transfer Conf.*, 2017, pp. 1–3.

[19] N. S. Jeong, S. Kim, H.-J. Lee, and J. H. Kim, "Wireless charging of a metal-encased device," *IEEE Trans. Antennas Propag.*, vol. 70, no. 1, pp. 654–663, Jan. 2022.

[20] N. S. Jeong and F. Carobolante, "Wireless charging of a metal-body device," *IEEE Trans. Microw. Theory Techn.*, vol. 65, no. 4, pp. 1077–1086, Apr. 2017.

[21] Z. Wang and A. Markham, "Wirelessly powered embedded sensor nodes for internal structural health monitoring," *IEEE Trans. Ind. Electron.*, to be published, doi: 10.1109/TIE.2020.3013536.

[22] R. H. Bhuiyan, M. R. Islam, J. M. Caicedo, and M. Ali, "A study of 13.5-MHz coupled-loop wireless power transfer under concrete and near metal," *IEEE Sensors J.*, vol. 18, no. 23, pp. 9848–9856, Dec. 2018.

[23] S.-H. Lee, M.-Y. Kim, B.-S. Lee, and J. Lee, "Impact of rebar and concrete on power dissipation of wireless power transfer systems," *IEEE Trans. Ind. Electron.*, vol. 67, no. 1, pp. 276–287, Jan. 2020.

[24] Y. Jang, J.-K. Han, J.-I. Baek, G.-W. Moon, J.-M. Kim, and H. Sohn, "Novel multi-coil resonator design for wireless power transfer through reinforced concrete structure with rebar array," in *Proc. IEEE 3rd Int. Future Energy Electron. Conf. ECCE Asia*, 2017, pp. 2238–2243.

[25] L. Qian, K. Cui, H. Xia, H. Shao, J. Wang, and Y. Xia, "An inductive power transfer system for powering wireless sensor nodes in structural health monitoring applications," *IEEE Trans. Microw. Theory Techn.*, vol. 70, no. 7, pp. 3732–3740, Jul. 2022.

[26] Y. Peng, W. Qi, Y. Chen, R. Mai, and U. K. Madawala, "Wireless sensor power supply based on eddy currents for structural health monitoring," *IEEE Trans. Ind. Electron.*, vol. 71, no. 7, pp. 7252–7261, Jul. 2024.

[27] Y. Peng, E. Ma, Q. Wang, Y. Chen, and R. Mai, "Effect of rebar array on IPT system for structural health monitoring sensor supply," in *Proc. IEEE 3rd Int. Conf. Ind. Electron. Sustain. Energy Syst.*, 2023, pp. 1–5.

[28] J. Park et al., "A resonant reactive shielding for planar wireless power transfer system in smartphone application," *IEEE Trans. Electromagn. Compat.*, vol. 59, no. 2, pp. 695–703, Apr. 2017.

[29] J. Park and S. Ahn, "A novel shielding coil for electromagnetic field(EMF) reduction of wireless power transfer in laptop computer," in *Proc. IEEE Wireless Power Transfer Conf.*, 2014, pp. 235–238.

[30] S. Kim, H.-H. Park, J. Kim, J. Kim, and S. Ahn, "Design and analysis of a resonant reactive shield for a wireless power electric vehicle," *IEEE Trans. Microw. Theory Techn.*, vol. 62, no. 4, pp. 1057–1066, Apr. 2014.

[31] S. Lee et al., "Low leakage electromagnetic field level and high efficiency using a novel hybrid loop-array design for wireless high power transfer system," *IEEE Trans. Ind. Electron.*, vol. 66, no. 6, pp. 4356–4367, Jun. 2019.

[32] B. H. Choi, V. X. Thai, E. S. Lee, J. H. Kim, and C. T. Rim, "Dipole-coil-based wide-range inductive power transfer systems for wireless sensors," *IEEE Trans. Ind. Electron.*, vol. 63, no. 5, pp. 3158–3167, May 2016.

[33] E. S. Lee, B. G. Choi, J. S. Choi, D. T. Nguyen, and C. T. Rim, "Wide-range adaptive IPT using dipole-coils with a reflector by variable switched capacitance," *IEEE Trans. Power Electron.*, vol. 32, no. 10, pp. 8054–8070, Oct. 2017.

[34] B. G. Choi, J. H. Kim, E. S. Lee, H. R. Kim, and C. T. Rim, "Optimal dipole-coil ampere-turns design for maximum power efficiency of IPT," *IEEE Trans. Power Electron.*, vol. 35, no. 7, pp. 7317–7327, Jul. 2020.

[35] C. Park, S. Lee, G.-H. Cho, and C. T. Rim, "Innovative 5-m-off-distance inductive power transfer systems with optimally shaped dipole coils," *IEEE Trans. Power Electron.*, vol. 30, no. 2, pp. 817–827, Feb. 2015.

Yuner Peng (Graduate Student Member, IEEE) was born in Sichuan Province, China, in 1998. She received the B.Sc. degree in electrical engineering in 2020 from the School of Electrical Engineering, Southwest Jiaotong University, Chengdu, China, where she is currently working toward the Ph.D. degree in electrical engineering.

From 2024 to 2025, she was a joint Ph.D. student founded by the China Scholarship Council with the University of Auckland, Auckland, New Zealand. Her main research interest includes wireless power transfer.

Endian Ma was born in Shandong Province, China, in 2000. He received the B.Sc. degree in electrical engineering from the School of Electrical Engineering, Qingdao University, Qingdao, China, in 2022. He is currently working toward the M.Sc. degree in electrical engineering with the Tangshan Graduate School, Southwest Jiaotong University, Chengdu, China.

His main research interest includes wireless power transfer.

Qi Wang received the B.Sc. degree in transport equipment and control engineering electrical in 2022 from the School of Mechanical Engineering, Southwest Jiaotong University, Chengdu, China, where she is currently working toward the M.Sc. degree in electrical engineering with the School of Electrical Engineering.

Her main research interest includes wireless power transfer.

Yang Chen (Senior Member, IEEE) received the B.Sc. degree in electrical engineering and automation and the Ph.D. degree in electrical engineering from Southwest Jiaotong University, Chengdu, China, in 2015 and 2020, respectively.

From 2018 to 2019, he was a Visiting Scholar founded by the China Scholarship Council with the Future Energy Electronics Center, Virginia Tech, Blacksburg, VA, USA. From 2020 to 2023, he was a Postdoctoral Researcher with Southwest Jiaotong University, Chengdu, China, where he is currently an Associate Researcher. His research focuses on wireless power transfer.

Dr. Chen was the recipient of the 2023 Outstanding Reviewer Award from IEEE TRANSACTIONS ON POWER ELECTRONICS.

Ruikun Mai (Senior Member, IEEE) received the B.Sc. and Ph.D. degrees in electrical engineering from the School of Electrical Engineering, Southwest Jiaotong University, Chengdu, China, in 2004 and 2010, respectively.

He is currently a Professor with the School of Electrical Engineering, Southwest Jiaotong University, Chengdu, China.

His research interests include wireless power transfer and its application in railway systems, power system stability, and control.

Udaya K. Madawala (Fellow, IEEE) received the B.Sc. (hons.) degree in electrical engineering from The University of Moratuwa, Moratuwa, Sri Lanka, in 1987, and the Ph.D. degree in power electronics from The University of Auckland, Auckland, New Zealand, in 1993, as a Commonwealth Doctoral Scholar.

He was employed by Fisher & Paykel Ltd., New Zealand, as a Research and Development Engineer to develop new technologies for motor drives. In 1997, he was with the Department of Electrical and Computer Engineering, The University of Auckland, where he is currently a Full Professor. His research interests include the fields of wireless power transfer, power electronics, V2G applications, and renewable energy.

Dr. Madawala is a Distinguished Lecturer of the IEEE Power Electronic Society and has more than 30 years of both industry and research experience in the fields of power electronics and energy. He was with the IEEE Power Electronics and Industrial Electronics Societies in numerous roles, relating to editorial, advisory, conference, technical committee, and chapter activities. He is currently an Associate Editor for IEEE TRANSACTIONS ON POWER ELECTRONICS, and a Member-at-Large of the Administrative Committee and the Oceania Liaison Chair of Membership Development Committee of the IEEE Power Electronics Society. He was the General Chair of the 2nd IEEE Southern Power Electronics Conference (SPEC)-2016, held in New Zealand, and is currently the Chair of the SPEC Steering Committee.